Scilight

Advanced Characterization

https://www.sciltp.com/journals/ac

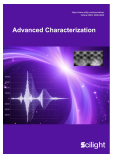

Supplementary Materials

Reversible Structure Formation in 4,4-Bipyridine—Fe 2D Metal-Organic Frameworks on Au(111)

Afra Gezmis [1], Simon Steinbach [1], Julien Steffen [2], Alisson Ceccatto [1], Isabela Tonon [3], Natalie Waleska-Wellnhofer [1], Abner de Siervo [3] and Hans-Peter Steinrück [1,*]

[1] Lehrstuhl für Physikalische Chemie II, Friedrich-Alexander-Universität Erlangen-Nürnberg, 91058 Erlangen, Germany
[2] Lehrstuhl für Theoretische Chemie, Friedrich-Alexander-Universität Erlangen-Nürnberg, 91058 Erlangen, Germany
[3] Institute of Physics Gleb Wataghin, University of Campinas, Campinas 13083-859, Brazil
* Correspondence: hans-peter.steinrueck@fau.de

How To Cite: Gezmis, A.; Steinbach, S.; Steffen, J.; et al. Reversible Structure Formation in 4,4-Bipyridine—Fe 2D Metal Organic Frameworks on Au(111). *Advanced Characterization* **2026**, *1*(1), 40–58.

1. Comparison of AFM and STM Data

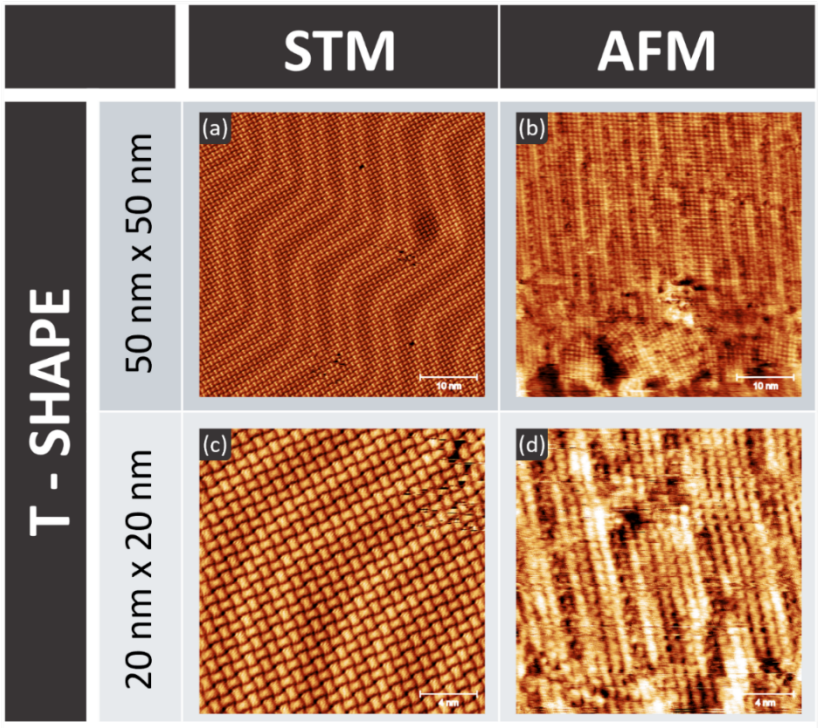

Figure S1. Saturated 4,4-bipy monolayer on Au(111), deposited at RT and cooled down to ~105 K for the measurements. Comparison of STM (**a**,**c**) and nc-AFM (**b**,**d**) images with sizes of 50 nm × 50 nm (top) and 20 nm × 20 nm (bottom), displaying a well-ordered quadratic lattice with two perpendicularly oriented molecules in a T-shape arrangement per unit cell; for details see manuscript. The STM data are from the same sample as those in Figure 1 in the manuscript. Measurement parameters are provided in Table S3.

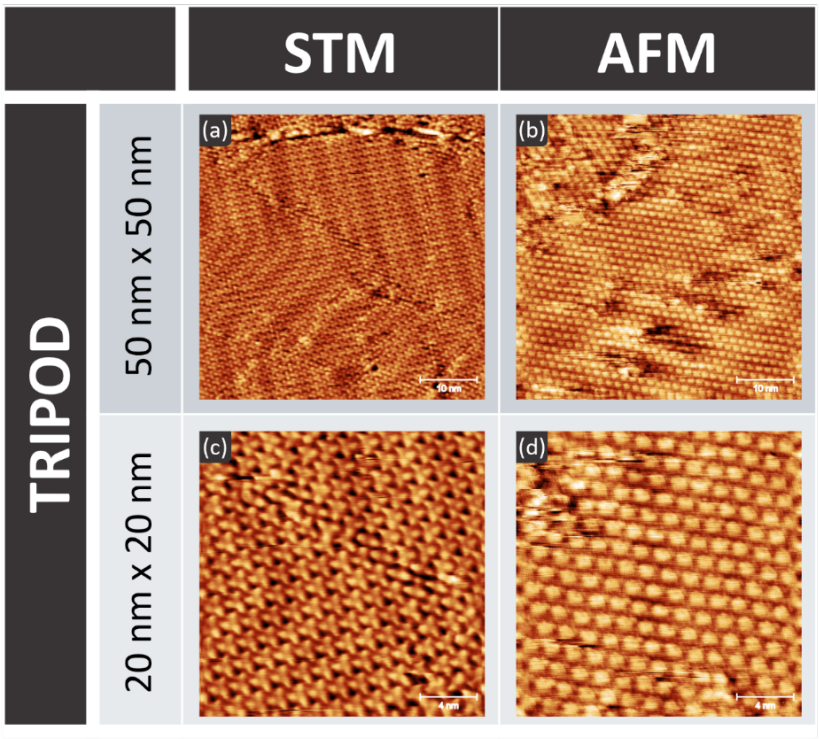

Figure S2. Tripod structure on Au(111), obtained after Fe deposition (~0.037 ML, equals ~0.51 Fe/nm^2) onto a saturated 4,4-bipy monolayer on Au(111) at RT, and cooling down to ~105 K. Comparison of STM (**a**,**c**) and nc-AFM (**b**,**d**) images with sizes of 50 nm × 50 nm (top) and 20 nm × 10 nm (bottom), displaying a well-ordered hexagonal lattice of triangular protrusions, which are assigned to tripods formed by three molecules coordinated by a central Fe atom; for details see manuscript. The STM data are from the sample as those in Figure 5 in the manuscript. Measurement parameters are provided in Table S3.

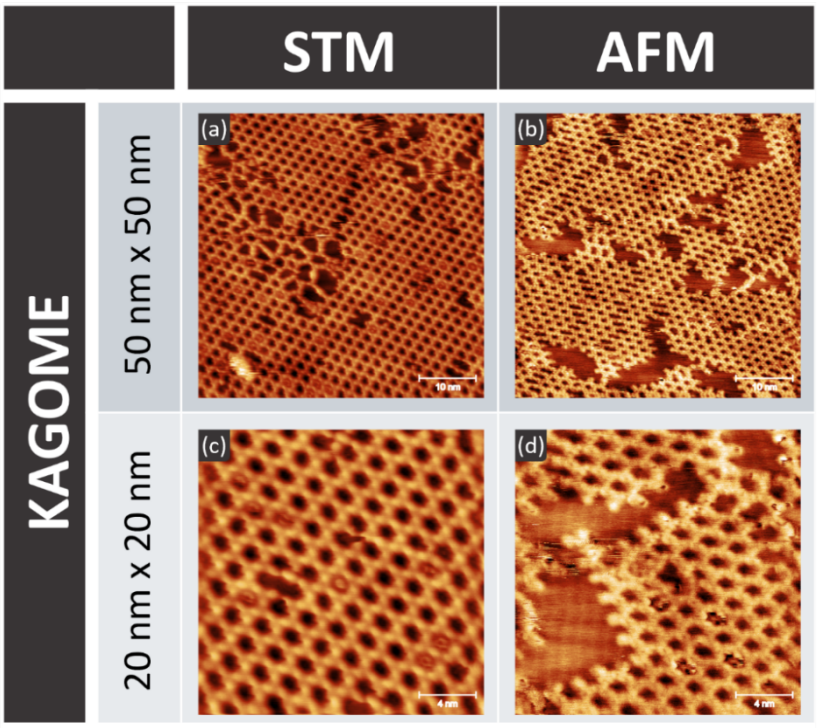

Figure S3. Hexagonal pore structure (Kagome lattice) on Au(111), obtained after annealing an extended tripod layer to 400 K for 10 min and cooling down to ~105 K, in a region of local high surface coverage displaying only the pore structure. Comparison of STM (**a**,**c**) and nc-AFM (**b**,**d**) images with sizes of 50 nm × 50 nm (top) and 20 nm × 20 nm (bottom); for details see manuscript. The STM data are from the same sample as those in Figure 8 in the manuscript. Measurement parameters are provided in Table S3.

2. Domains of T-Shape Structure

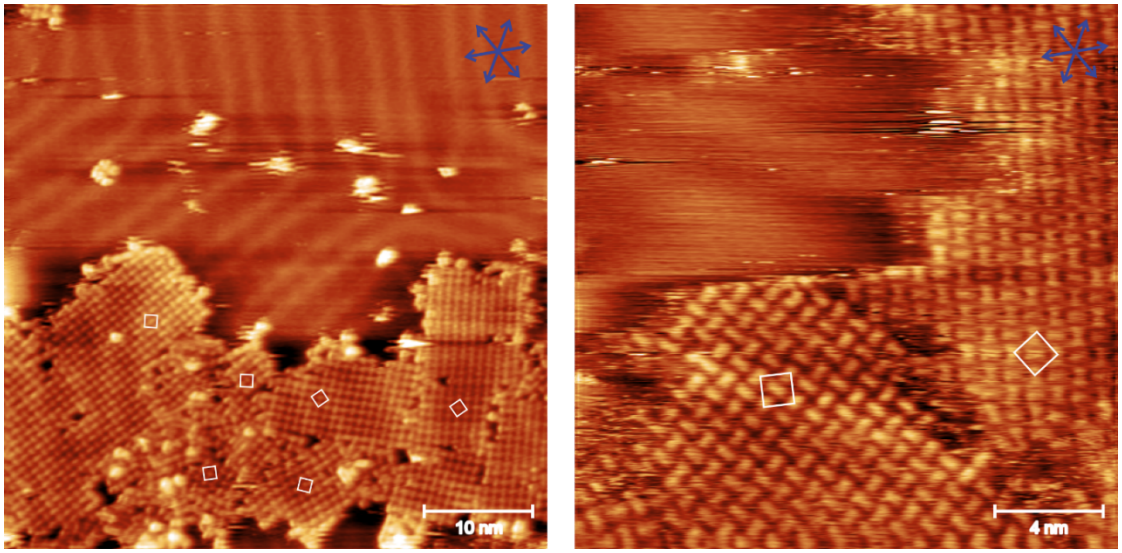

Figure S4. Exemplary STM images (left: 50 nm × 50 nm, right: 20 nm × 20 nm) showing coexisting domains with different orientations of the T-shape structure formed by 4,4-bipy on Au(111). The Au(111) substrate directions are indicated by blue arrows in the top right corners. Measurement parameters are provided in Table S3.

3. Low-Energy Electron Diffraction Data

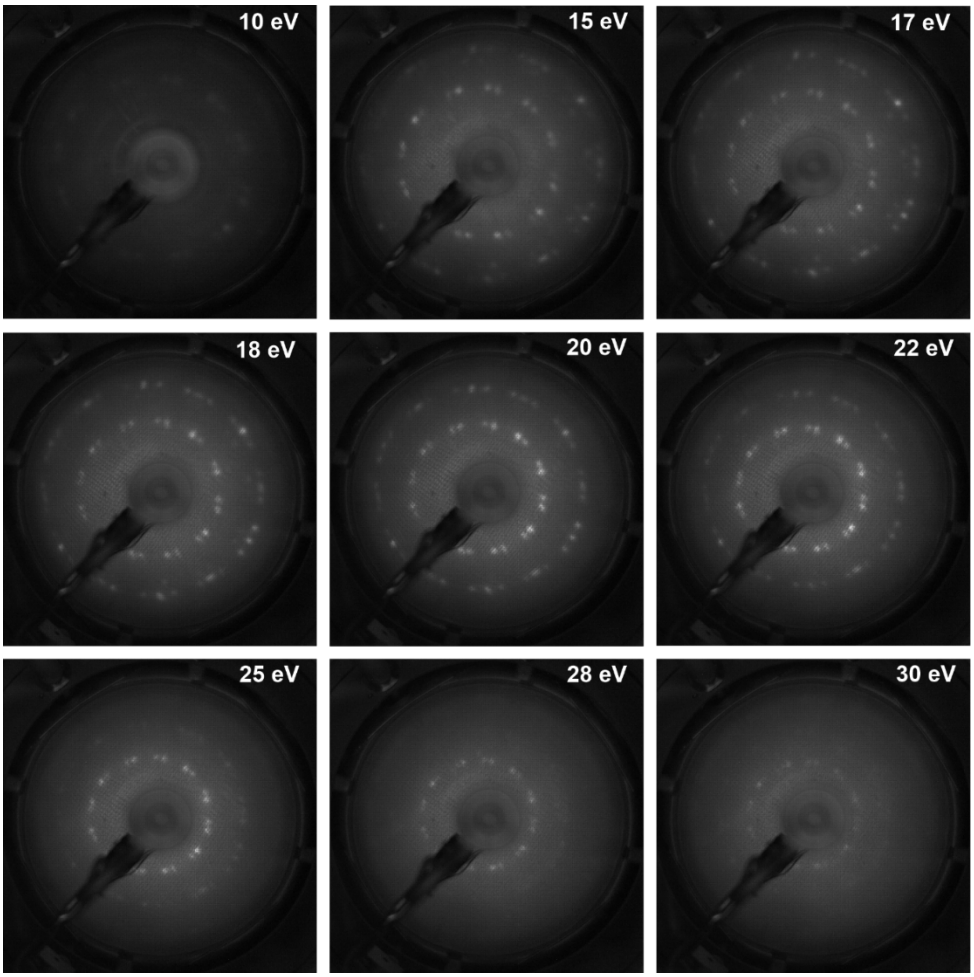

Figure S5. LEED patterns recorded of a saturated 4,4-bipy film on Au(111) arranged in a T-shape pattern at different beam energies (given in top right corner of each image).

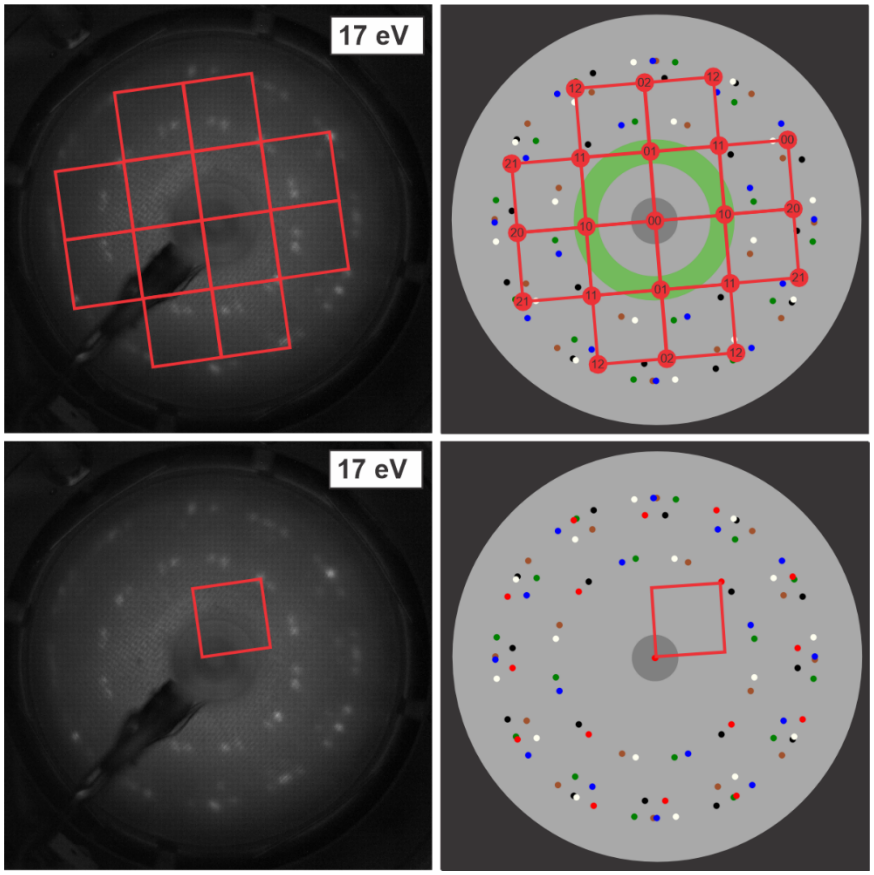

Figure S6. LEED pattern of a T-shape 4,4-bipy monolayer on Au(111) recorded at a beam energy of 17 eV (left). Simulated LEED pattern in shown on the right. TOP: Quadratic pattern of one domain is marked by a red grid in both the LEED and the simulated pattern. Reflexes are numbered in the grid for the simulated pattern (XY). Due to the mirror glide plane symmetry of the T-shape structure the 10 and 01 diffraction spots are not visible. Therefore, all spots on the green circle are not seen in the diffraction pattern. A total of 6 domains gives then the resulting diffraction pattern shown again for comparison (bottom) A single exemplary unit cell is marked with a red square in both the LEED (left) and simulated pattern (right).

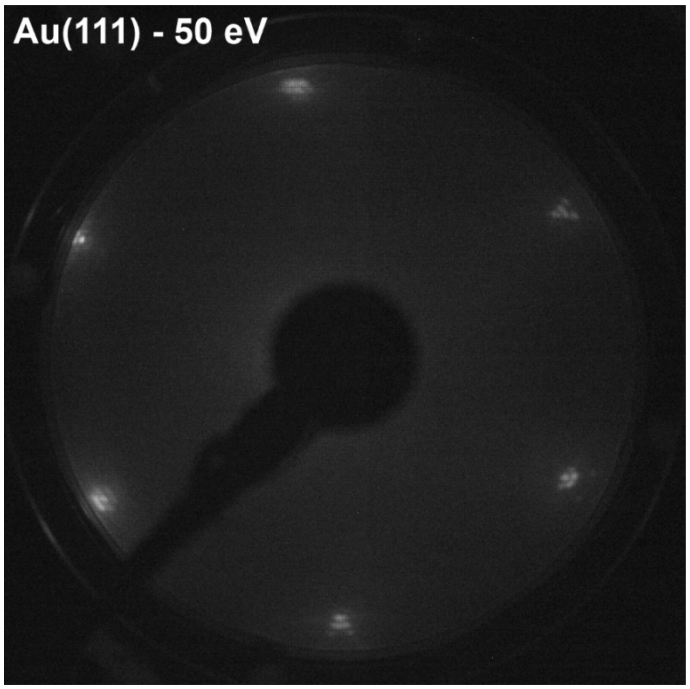

Figure S7. LEED pattern of the clean Au(111) recorded at a beam energy of 50 eV. The herringbone reconstruction leads to a splitting of the spots. Notably, at this beam energy the adsorbate superstructure spots would be too weak to be seen.

4. Additional STM Data of Tripod Structure Formation

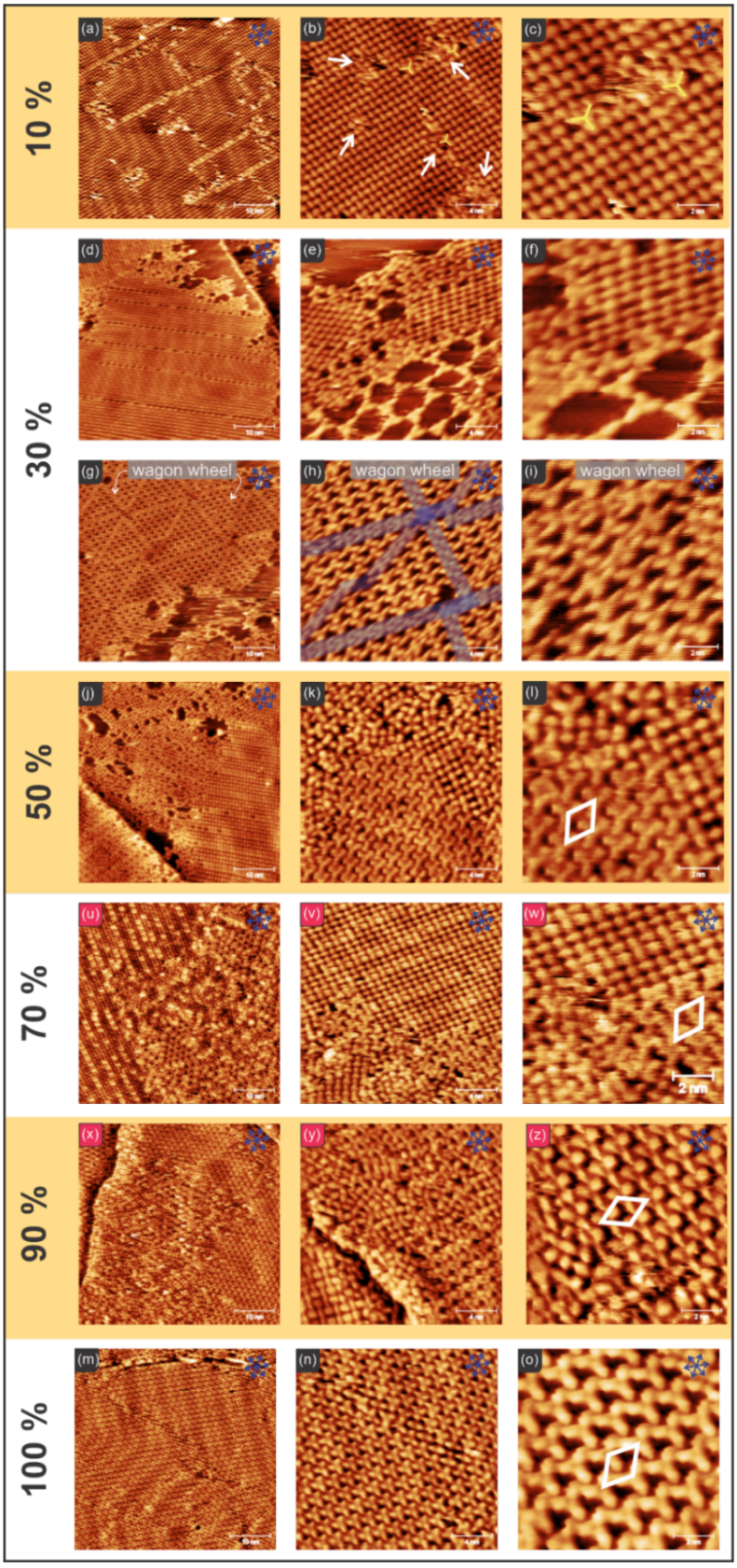

Figure S8. STM images of a 4,4-bipy monolayer after adding different doses of Fe at RT. An Fe dose of 100% (**m**–**o**; 300 sec Fe evaporation, I_{flux} = 1.0 nA) equals ~0.037 ML or ~0.51 Fe/nm^2. The image sizes decrease (left to right) from 50 nm × 50 nm to 20 nm × 20 nm, and 10 nm × 10 nm. (**a**–**c**) 10% (30 sec Fe): Fe-induced defect sites are marked with white arrows, first tripods with yellow tripod bars. (**d**–**i**) 30% (90 sec Fe): the upper panel shows a region with disordered tripods at the edges of the T-shape structure, and tripods partially arranging in a pore-like

orientation (note that these pores are different from the hexagonal pores in Figure 4); the lower panel shows a region of tripods in a wagon wheel structure, with mirror twin boundaries marked in blue (**h**). (**j**–**l**) 50% (150 sec Fe): Coexistence of ordered tripod and T-shape structures, and disordered tripods (**k**, top left). The tripod unit cell is marked in white. (**u**–**w**) 70% (210 sec Fe): overall very similar to 50%. (**x**–**z**) 90% (270 s Fe): already very similar to 100%. (**m**–**l**) 100% Fe dose (see above). The tripod unit cell is marked in white. Images (**a**–**l**) were recorded on one sample by successively adding Fe, while (**m**–**o**) were recorded on different samples. The Au(111) substrate directions are indicated by blue arrows in the top right corners. All images were recorded at ~105 K. For measurement parameters, please refer to Table S3.

5. DFT Calculations

Calculation details:

In order to obtain some insight into the lateral interactions in the adsorbed layers, which are driving the formation of the observed structures, we carried out periodic DFT modeling of the different systems. The calculations were performed with the VASP code, in which a plane wave basis set for the description of the valence electrons is used in combination with the projector augmented wave (PAW) method for the representation of the atomic cores [1–3]. It is important to note here that neglecting the interaction with substrate is a crude estimation, but including it would be computationally extremely demanding and is out of the scope of the present study. Despite these limitations, the calculations proved to be very helpful to understand the observed behavior.

The kinetic energy cutoff was chosen to be 500 eV for unit cell relaxations and 450 eV for optimizations of atomic positions in fixed unit cells, exchange correlation effects were treated with the PBE functional [4]. The DFT D3 correction was used for the better description of dispersion interactions [5,6].

The movable atoms were relaxed until all their gradient components were below 0.02 eV/Å.

Four different structures were looked at:

(1) The **hexagonal** pattern, with three 4,4-bipyridine molecules and two Fe atoms per unit cell,
(2) the **tripod** pattern, with one tripod with a Fe atom and three 4,4-bipyridine molecules per cell,
(3) the **T-shape** pattern, containing two 4,4-bipyridine molecules per square cell,
(4) the **long-pore** pattern, containing 12 4,4-bipyridine molecules and 10 Fe atoms in the scaffold and three or twelve additional 4,4-bipyridine molecules in the cell.

A single 4,4-bipyridine molecule and a tripod molecule were further optimized in the gas phase, in cubic cells with edge lengths of 20 Å for the former and 30 Å for the latter.

For the relaxation of the patterns, the shape of the unit cell was allowed to change for the tripod pattern, while only the total volume of the unit cells was allowed to change for the other three patterns. For the tripod patterns, all atoms were forced to stay on the x-y plane, by setting the dynamics flags of the z coordinates to F. To obtain the best structure of the tripod pattern, 12 different initial rotation angles of the tripods within the hexagonal unit cell were optimized, ranging from 0° to 22°. For this set of calculations, the unit cell shape was open for optimization as well. Since higher rotation angles led to increased steric demands, the initial unit cell sizes were gradually increased to avoid collisions of atoms. The results are listed in detail in Table S2, while only the results for 0°, having the lowest energy, are presented in the main manuscript.

Brillouin zone sampling was done with a Γ-containing 2 × 2 × 1 k-point mesh for the hexagonal, tripod, and square patterns and at the Γ-point only for the long-pore pattern. A Gaussian scheme with a broadening of 0.04 eV was applied to smear the electronic states for all calculations. All calculations were done spin-polarized.

Results:

The optimized structures of the hexagonal, tripod, and square patterns are shown in Figure 1.

The formation energy of the **hexagonal pattern** is **7.84 eV** per unit cell (**3** 4,4-bipyridine and **2** Fe atoms), that is, **2.61 eV** per 4,4-bipy molecule; it is thus thermodynamically very stable. The lattice distance in the hexagonal pattern is **1.943 nm**, and the nearest distance between Fe atoms is 1.122 nm

The formation energy of the **tripod pattern** in the gas phase (**3** 4,4-bipyridine and **1** Fe atom in a planar configuration) is **3.755 eV**, that is, **1.251 eV** per molecule; the formation energy of the tripod pattern (compared to isolated gas phase tripod units) is an additional **0.625 eV** per tripod, that is, **0.208 eV** per molecule (see Table 1), hence the pattern is thermodynamically favored, too, although only slightly; the total formation energy of the tripod pattern sums up to **1.46 eV** per molecule, with a lattice distance is **1.507** nm. The unit cell of the tripod pattern has an angle of 60.021°, hence it is almost exactly hexagonal. The 4,4-bipyridine units in the hexagonal cell are aligned parallel to the x-y plane, as it was forced by the calculation settings.

In the experiment, the tripods appear to be rotated in the unit cell by 12–15°. We thus performed an additional set of calculations considering different rotations of the tripod pattern with respect to the direct connection line between Fe atoms (Table S3). Calculations were performed for fixed rotation angles of 2, 4, 6, 8, 10, 12, 14, 16, 18, 20, and 22°, but otherwise optimized—see Table S2. With increasing rotation angle, the unit cell size increased up to a lattice constant of 1.94 nm (for 22°) and at the same time the formation energy decreased from 0.208 to 0.081 eV per molecule; this indicates that with the enforced planar geometry and neglection of the substrate, the calculations do not reproduce the rotation of the molecules well. Nevertheless, it allows for an estimate of the energetics of the structure formation.

In the **square unit cell (T-shape structure)**, the formation energy is **0.92 eV** per unit cell of two molecules, that is, **0.462 eV** per molecule, and thus between the hexagonal and the tripod patterns. One square unit cell containing two molecules has an edge length of **1.113 nm**. The distance between two N atoms with an orthogonal 4,4-bipyridine between them is 0.859 nm, while a molecule is 0.715 nm long (N to N distance).

The optimized **empty long-pore structure** is shown in Figure 2a, the optimized pore-filled structure with three 4,4-bipyridine molecules is shown in Figure 2b. Initially, the three molecules were but in the row as shown, but with dihedral angles of ca. 60° between both aromatic units. Hence, this angle shrinks a bit during the optimization (to ca. 41.8°), see Figure 2c, but still significantly deviates from the perfect planar structure of the gas phase molecule. The distance between two molecules is 0.43 nm, while the distance between the outer molecules and the H atoms of the pore scaffold is ca. 0.33 nm. It can further be seen that the centers of masses of the molecules are located exactly in the center of mass plane of the pore scaffold. Further, the bipyridine units of the pore nearest to the inserted molecules are inclined a bit as well, by ca 20° (left and right) and 10° (top-left and top-right) (looking at Figure 2b). The formation energy of the empty pore structure is **2.89 eV**, thus even a bit larger than the hexagonal structure, making it the thermodynamically most stable of all three studied adsorption patterns.

The distances between the Fe atoms in the long-pore structure are around 1.10 nm for the vertical stripes in Figure 2, while they are slightly larger (1.116 nm) in the rotated stripes on the top and bottom. In the long-pore structure filled with 12 4,4-biypridine molecules, the distances between N atoms of neighboring molecules in the columns are 0.33 nm between the first and second and between the third and fourth, while it is a bit longer (0.43 nm) between the second and the third molecule.

It should be noted that the bipyridine units of the filled long-pore systems started to rotate more and more at a late stage of the geometry optimization, which led to increasing problems with the self-consistent field convergence of the DFT calculation, probably due to the lower symmetry of the ligands along the Fe atoms (these are spin-polarized and therefore difficult to calculate at the first place). It was assumed that this rotation is mostly due to the absence of a metal surface below the system (which would probably stabilize the planar pore system), and thus mostly a computational artifact. The geometry optimizations are therefore stopped after ca. 400 steps and the total energy of the last considered steps was taken to calculate the insertion energy per bipyridine molecule.

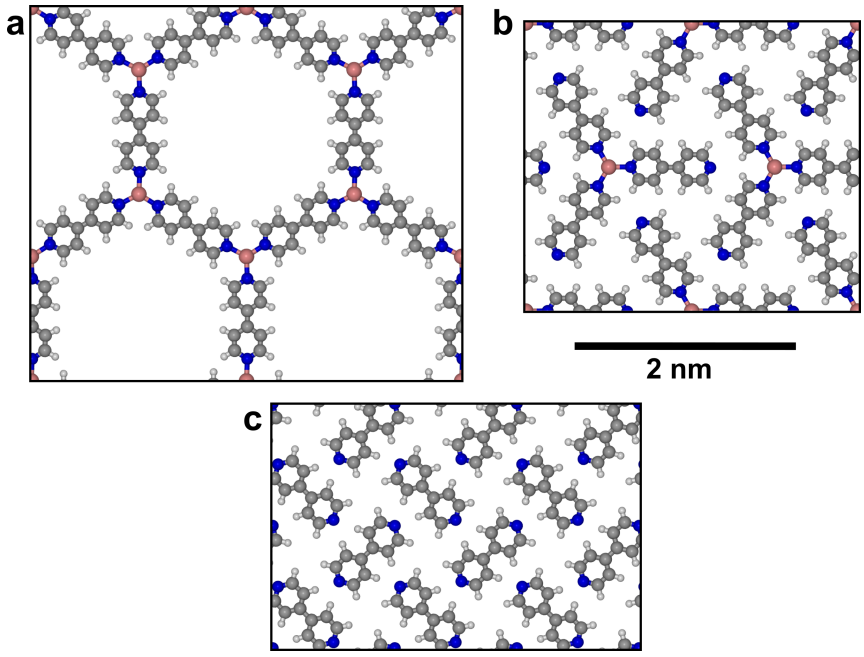

Figure S9. Optimized geometries of the (**a**) hexagonal pattern; (**b**) the tripod pattern with a rotation angle of 0°; and (**c**) the square pattern.

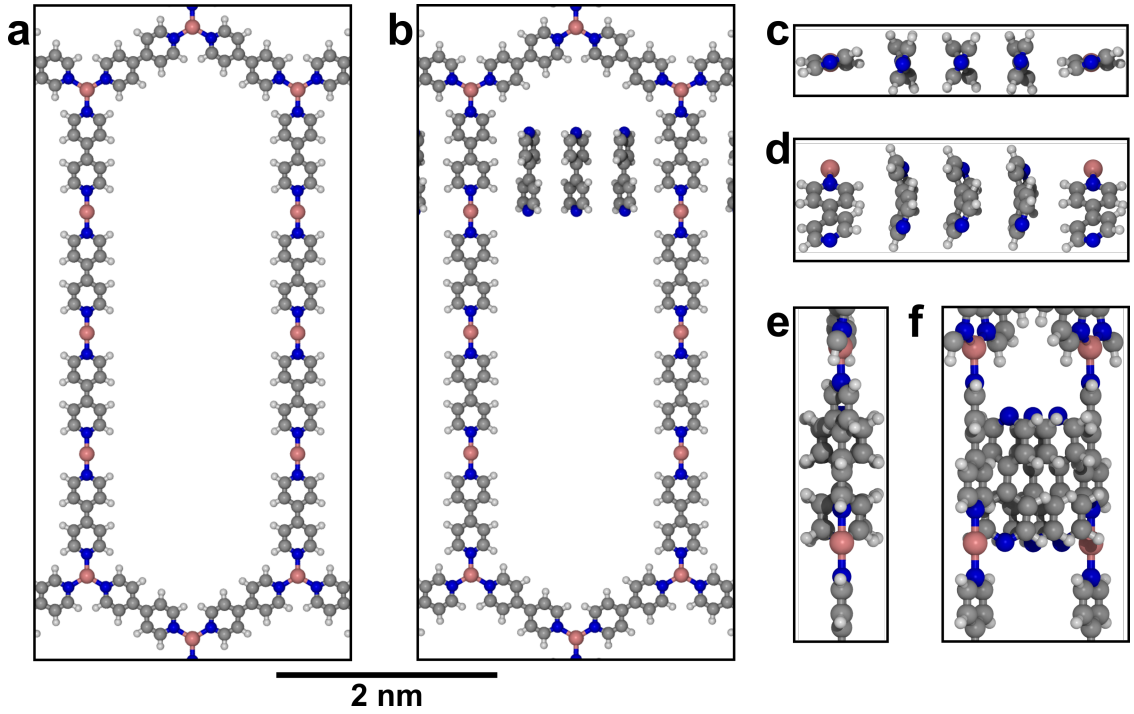

Figure S10. Optimized geometry of the long-pore pattern. Shown are the geometries of (**a**) the empty pore and (**b**) the pore filled with three 4,4-bipyridine molecules. Views from the lower edge of the unit cell along the y axis are shown in (**c**) (perspective parallel to the x-y plane) and (**d**) (perspective 20° towards the x-y plane). Views from the left edge of the unit cell along the x axis are shown in (**e**) (perspective parallel to the x-y plane) and (**f**) (perspective 20° towards the x-y plane).

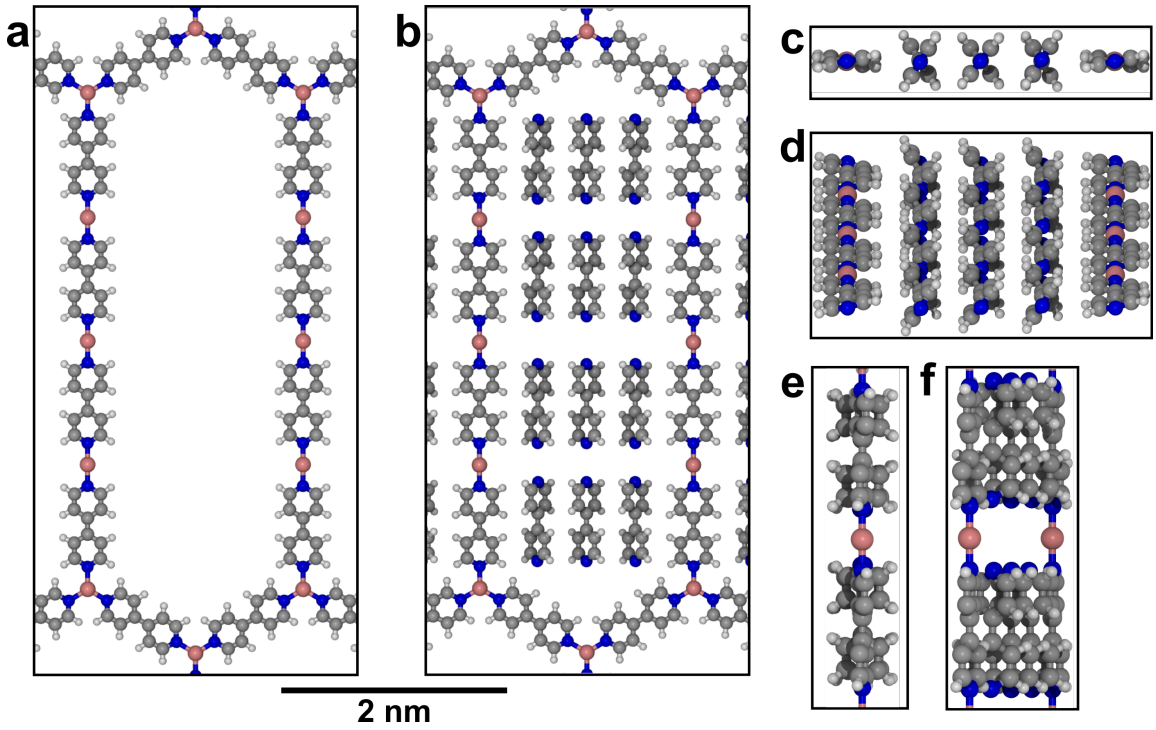

Figure S11. Optimized geometry of the long-pore pattern. Shown are the geometries of (**a**) the empty pore and (**b**) the pore filled with twelve 4,4-bipyridine molecules. Views from the lower edge of the unit cell along the y axis are shown in (**c**) (perspective parallel to the x-y plane) and (**d**) (perspective 20° towards the x-y plane). Views from the left edge of the unit cell along the x axis are shown in (**e**) (perspective parallel to the x-y plane) and (**f**) (perspective 20° towards the x-y plane).

Table S1. Absolute and relative DFT energies of the optimized structures. The per molecule energies (in bold) always refer to the relative formation energies of the structures per 4,4-bipyridine units, irrespective of the number of Fe atoms in the structures.

System	Energy (eV)	Formation Energy (Gas Phase)	Formation Energy (eV) (Gas Phase) Per Molecule	Formation Energy (eV) (Surface)	Formation Energy (eV) (Surface) Per Molecule	Total Formation Energy (eV) Per Molecule
4,4-biypridine (gasphase)	−135.882					
Fe atom (gasphase)	−3.377					
Tripod (gasphase, planar)	−414.778					
Hexagonal	−422.239	7.838	**2.613**			**2.613**
Tripod–0°	−415.403	3.755	**1.251**	0.625	**0.208**	**1.460**
Square	−272.689			0.924	**0.462**	**0.462**
Long-pore (empty)	−1699.093	34.736	**2.894**			**2.894**
Long-pore (filled,3)	−2108.314			1.575	**0.525**	
Long-pore (filled,12)	−3334.862			5.185	**0.432**	

Table S2. Absolute and relative energies of the tripod structure for different rotations of the tripods with respect to the unit cell. The unit cell shapes were open for optimization as well, but led to geometries very close to hexagonal in all cases. The systems are named according to the initial rotation angles of the tripods.

System	Rotation Angle (Optimized)	Unit Cell Size (nm)	Energy (eV)	Formation Energy (eV) (Surface)	Formation Energy (eV) (Surface) Per Molecule
0°	1.11	1.507	−415.403	0.625	0.208
2°	1.88	1.499	−415.382	0.604	0.201
4°	4.70	1.584	−415.275	0.497	0.166
6°	6.26	1.612	−415.264	0.486	0.162
8°	8.36	1.635	−415.318	0.540	0.180
10°	8.82	1.644	−415.313	0.535	0.178
12°	10.07	1.656	−415.299	0.521	0.174
14°	14.11	1.786	−415.096	0.318	0.106
16°	15.74	1.813	−415.077	0.299	0.100
18°	16.94	1.832	−415.070	0.292	0.097
20°	18.14	1.860	−415.063	0.285	0.095
22°	22.23	1.929	−415.062	0.284	0.095
24°	23.21	1.935	−415.020	0.242	0.081

6. Measurement Parameters and Preparation Details

Table S3. Preparation and measurement details of shown STM images. T_{evap}: temperature of the sample during the 4,4-bipy evaporation, T_{max}: highest temperature the sample has experienced during the time of the scan (indicated the last annealing process), T_{meas}: temperature at which the image was recorded. For STM, the tunneling current (I_T), and for AFM, the frequency shift (Df) is given. For images not labeled as (a), (b), (c), etc. the following identification markers are used: t = top, m= middle, b = bottom, r = right, l = left. Post-measurement corrections such as drift correction or cutting of the originally measured STM image are labeled in the "Note-column".

Figure	Filename	T_{evap}	T_{max}	T_{meas}	V_{Bias}	I_T or Df	Note
1 (a)	20250312_33-1	305 K	305 K	103 K	−0.80 V	0.80 nA	
1 (b)	20250312_36-1	305 K	305 K	103 K	−0.80 V	0.80 nA	
1 (c)	20250312_31-1	305 K	305 K	103 K	−0.80 V	0.80 nA	cut
1 (d)	20250312_33-1	305 K	305 K	103 K	−0.80 V	0.80 nA	FFT
2 (t,l)	20250729_16-1	300 K	300 K	105 K	−1.40 V	0.30 nA	
2 (t,r)	20250730_87-1	300 K	370 K	103 K	−1.40 V	0.60 nA	
2 (b,r)	20250731_14-1	300 K	412 K	104 K	−1.40 V	0.40 nA	
2 (b,l)	20250731_69-1	300 K	450 K	105 K	−1.40 V	0.40 nA	
3 (a)	20250509_3-1	310 K	310 K	104 K	−0.60 V	0.70 nA	
3 (b)	20250509_4-1	310 K	310 K	104 K	−1.60 V	0.08 nA	
3 (c)	20250509_36-1	310 K	310 K	104 K	−1.40 V	0.08 nA	
3 (d)	20250401_4-1	300 K	300 K	103 K	−0.80 V	0.80 nA	
3 (e)	20250401_6-1	300 K	300 K	103 K	−0.80 V	0.40 nA	
3 (f)	20250401_7-1	300 K	300 K	103 K	−0.80 V	0.60 nA	
3 (g)	20250417_3-1	300 K	300 K	104 K	−0.60 V	0.60 nA	
3 (h)	20250417_14-1	300 K	300 K	104 K	−0.70 V	0.50 nA	
3 (i)	20250417_10-10	300 K	300 K	104 K	−0.70 V	0.40 nA	
4 (a)	20250422_16-1	300 K	300 K	104 K	−0.70 V	0.60 nA	
4 (b)	20250422_16-1	300 K	300 K	104 K	−0.70 V	0.60 nA	cut3
4 (c)	20250422_16-1	300 K	300 K	104 K	−0.70 V	0.60 nA	cut2
4 (d)	20250422_16-1	300 K	300 K	104 K	−0.70 V	0.60 nA	cut

Table S3. *Cont.*

Figure	Filename	T_{evap}	T_{max}	T_{meas}	V_{Bias}	I_T or Df	Note
5 (a)	20250523_45-1	297 K	297 K	103 K	−1.40 V	0.08 nA	
5 (b)	20250523_44-1	297 K	297 K	103 K	−1.40 V	0.08 nA	
5 (d)	20250523_44-1	297 K	297 K	103 K	−1.40 V	0.08 nA	FFT
5 (c)	20250519_34-1	283 K	300 K	103 K	−1.40 V	0.20 nA	cut
6 (a)	20251028_44-1	327 K	327 K	106 K	−1.40 V	0.60 nA	
6 (b)	20251028_41-1	327 K	327 K	106 K	−1.40 V	0.60 nA	
6 (c)	20251028_41-1	327 K	327 K	106 K	−1.40 V	0.60 nA	cut
6 (d)	20251104_10-1	327 K	327 K	108 K	−1.40 V	0.50 nA	
6 (e)	20251104_12-1	327 K	327 K	108 K	−1.40 V	0.50 nA	
6 (f)	20251104_12-1	327 K	327 K	108 K	−1.40 V	0.50 nA	cut
6 (g)	20251104_24-3	327 K	327 K	108 K	−1.40 V	0.50 nA	
6 (h)	20251104_27-1	327 K	327 K	108 K	−1.40 V	0.50 nA	
6 (i)	20251104_27-1	327 K	327 K	108 K	−1.40 V	0.50 nA	cut
6 (j)	20251105_28-1	327 K	327 K	105 K	−1.40 V	0.50 nA	
6 (k)	20251105_37-1	327 K	327 K	105 K	−1.40 V	0.50 nA	
6 (l)	20251105_37-1	327 K	327 K	105 K	−1.40 V	0.50 nA	cut
6 (m)	20250523_45-1	297 K	297 K	103 K	−1.40 V	0.08 nA	
6 (n)	20250523_44-1	297 K	297 K	103 K	−1.40 V	0.08 nA	
6 (o)	20250519_34-1	283 K	300 K	103 K	−1.40 V	0.20 nA	cut
7 (a)	20251023_28-1	300 K	410 K	104 K	−1.40 V	0.40 nA	
7 (b)	20251023_32-1	300 K	410 K	104 K	−1.40 V	0.40 nA	
7 (c)	20251023_34-1	300 K	410 K	104 K	−1.40 V	0.40 nA	
8 (a)	20250526_82-2	297 K	342 K	104 K	−1.40 V	0.20 nA	FFT shown as (d)
8 (b)	20250520_52-1	283 K	342 K	103 K	−1.40 V	0.30 nA	Drift corrected
8 (c)	20251209_37-9	310 K	420 K	106 K	−1.40 V	0.80 nA	
8 (d)	20250520_55-2	283 K	342 K	103 K	−1.40 V	0.30 nA	FFT
9 (a)	20250312_36-1	305 K	305 K	103 K	−0.80 V	0.80 nA	cut
9 (b)	20250519_34-1	283 K	300 K	103 K	−1.40 V	0.20 nA	cut
9 (c)	20251209_37-9	310 K	420 K	106 K	−1.40 V	0.80 nA	
10 (l)	20250523_44-1	297 K	297 K	103 K	−1.40 V	0.08 nA	
10 (r,t)	20251217_30-1	314 K	423 K	105 K	−1.40 V	0.40 nA	
10 (r,b)	20251002_28-7	318 K	416 K	106 K	−1.40 V	0.40 nA	
S1 (a)	20250312_33-1	305 K	305 K	103 K	−0.80 V	0.80 nA	
S1 (b)	20260219_3-16	287 K	287 K	103 K	−1.00 V	−600 Hz	AFM
S1 (c)	20250312_34-1	305 K	305 K	103 K	−0.80 V	0.80 nA	
S1 (d)	20260219_3-24	287 K	287 K	103 K	−1.00 V	−600 Hz	AFM
S2 (a)	20250323_45-1	297 K	297 K	103 K	−1.40 V	0.08 nA	
S2 (b)	20260216_8-1	289 K	400 K	105 K	−1.40 V	−500 Hz	AFM
S2 (c)	20250323_44-1	297 K	297 K	103 K	−1.40 V	0.08 nA	
S2 (d)	20260216_6-1	289 K	400 K	105 K	−1.40 V	−500 Hz	AFM
S3 (a)	20250526_66-1	297 K	340 K	104 K	−1.40 V	0.20 nA	
S3 (b)	20250528_13-4	297 K	340 K	103 K	−0.60 V	−600 Hz	AFM
S3 (c)	20250526_82-2	297 K	340 K	104 K	−1.40 V	0.20 nA	
S3 (d)	20250528_14-2	297 K	340 K	103 K	−0.60 V	−600 Hz	AFM
S4 (l)	20250731_9-1	300 K	400 K	104 K	−1.40 V	0.40 nA	
S4 (r)	20250408_2-9	163 K	163 K	104 K	−0.60 V	0.50 nA	
S8 (a)	20251028_44-1	327 K	327 K	106 K	−1.40 V	0.60 nA	
S8 (b)	20251028_41-1	327 K	327 K	106 K	−1.40 V	0.60 nA	
S8 (c)	20251028_41-1	327 K	327 K	106 K	−1.40 V	0.60 nA	
S8 (d)	20251104_10-1	327 K	327 K	108 K	−1.40 V	0.50 nA	
S8 (e)	20251104_12-1	327 K	327 K	108 K	−1.40 V	0.50 nA	
S8 (f)	20251104_12-1	327 K	327 K	108 K	−1.40 V	0.50 nA	
S8 (g)	20251104_24-3	327 K	327 K	108 K	−1.40 V	0.50 nA	
S8 (h)	20251104_27-1	327 K	327 K	108 K	−1.40 V	0.50 nA	
S8 (i)	20251104_27-1	327 K	327 K	108 K	−1.40 V	0.50 nA	cut
S8 (j)	20251105_28-1	327 K	327 K	105 K	−1.40 V	0.50 nA	
S8 (k)	20251105_37-1	327 K	327 K	105 K	−1.40 V	0.50 nA	
S8 (l)	20251105_37-1	327 K	327 K	105 K	−1.40 V	0.50 nA	
S8 (u)	20251106_47-1	327 K	327 K	105 K	−1.40 V	0.60 nA	
S8 (v)	20251106_62-1	327 K	327 K	105 K	−1.40 V	0.60 nA	
S8 (w)	20251106_62-1	327 K	327 K	105 K	−1.40 V	0.60 nA	cut
S8 (x)	20251107_36-1	327 K	327 K	104 K	−1.40 V	0.70 nA	
S8 (y)	20251107_59-8	327 K	327 K	104 K	−1.40 V	0.70 nA	
S8 (z)	20251107_40-1	327 K	327 K	104 K	−1.40 V	0.70 nA	
S8 (m)	20250523_45-1	297 K	297 K	103 K	−1.40 V	0.08 nA	
S8 (n)	20250523_44-1	297 K	297 K	103 K	−1.40 V	0.08 nA	
S8 (o)	20250519_34-1	283 K	300 K	103 K	−1.40 V	0.20 nA	

References

1. Kresse, G.; Furthmüller, J. Efficient iterative schemes for ab initio total-energy calculations using a plane-wave basis set. *Phys. Rev. B* **1996**, *54*, 11169–11186.
2. Kresse, G.; Furthmüller, J. Efficiency of ab-initio total energy calculations for metals and semiconductors using a plane-wave basis set. *Comput. Mater. Sci.* **1996**, *6*, 15–50.
3. Kresse, G.; Joubert, D. From Ultrasoft Pseudopotentials to the Projector Augmented-Wave Method. *Phys. Rev. B* **1999**, *59*, 1758–1775.
4. Perdew, J.P.; Burke, K.; Ernzerhof, M. Generalized Gradient Approximation Made Simple. *Phys. Rev. Lett.* **1996**, *77*, 3865–3868.
5. Grimme, S.; Antony, J.; Ehrlich, S.; et al. A consistent and accurate ab initio parametrization of density functional dispersion correction (DFT-D) for the 94 elements H-Pu. *J. Chem. Phys*. **2010**, *132*, 154104.
6. Grimme, S.; Ehrlich, S.; Goerigk, L. Effect of the damping function in dispersion corrected density functional theory. *J. Comput. Chem*. **2011**, *32*, 1456–1465.